



Water-assisted ions *in situ* intercalation for porous polymeric graphitic carbon nitride nanosheets with superior photocatalytic hydrogen evolution performance

Longtao Ma, Huiqing Fan*, Ju Wang, Yuwei Zhao, Hailin Tian, Guangzhi Dong

State Key Laboratory of Solidification Processing, School of Materials Science and Engineering, Northwestern Polytechnical University, Xi'an 710072, China



ARTICLE INFO

Article history:

Received 24 December 2015
Received in revised form 29 February 2016
Accepted 2 March 2016
Available online 6 March 2016

Keywords:

Porous carbon nitride nanosheets
In situ ion-intercalated exfoliation
Hydrogen production
Electronic structure

ABSTRACT

Two-dimension layered polymeric carbon nitride possessing unique electronic structure and high specific surface area exhibits immense potentials for visible light driven photocatalytic activity for hydrogen production by the decomposition of water molecules. Herein, porous polymeric carbon nitride nanosheets were obtained by lithium chloride ions *in situ* intercalating bulk materials in thermal polycondensation process and followed by liquid exfoliation in water. The porous nanosheets show two-dimension layered structure with the thickness of 2–3 nm, a high density in-plane pores with 2–3 nm diameter, a higher surface area ($186.3 \text{ m}^2 \text{ g}^{-1}$), enlarged bandgap (by 0.16 eV), prolonged charge carrier lifetime, enhanced electronic transport ability, increased charge carrier density and improved photocurrent responses, which could significantly give rise to photocatalytic activity. The results highlight the crucial role of 2D porous structure, high specific surface area and unique electronic structure on the photocatalytic performance of polymeric carbon nitride materials.

© 2016 Elsevier B.V. All rights reserved.

1. Introduction

The exploration of highly efficient photocatalyst for hydrogen production from water splitting is regarded as a promising strategy for converting sustainable solar energy to hydrogen energy [1]. Photocatalytic efficiency is dominated by photo-generation of charge carriers in semiconductor, which is determined by four major contributors. In sequence, they are efficiencies of (1) light absorption, (2) exciton diffusion, (3) charge formation and separation and finally (4) charge transport and collection [2]. Hence, searching superior photocatalyst to improve photo-induced charge carrier efficiency in the process of photocatalytic reaction is necessary. Carbon nitrides, a great semiconductor has attracted considerable interesting as a promising metal-free visible-light photocatalyst owing to the merits of unique electronic structure, abundance, high stability and chemical tenability [3,4]. The CNs based on heptazine building blocks, known as melon is often called graphitic carbon nitride ($g\text{-C}_3\text{N}_4$, noted as CN in this paper) and its structure is similar to graphite [5,6]. The crystal structure of polymeric graphitic carbon nitride is depicted in Fig. 1. The layers are composed of tri-*s*-triazine motifs and stacked in an ABA-fashion

combined by weak van der Waals forces [7]. In the past year, many strategies were conducted to enhance photocatalytic activity of CNs, such as doping heteroatoms [8,9], constituting heterojunction [10–13], sensitizing with organic dyes [14] and controlling morphology [15–19]. For semiconductors, morphology is an important parameter due to its remarkable effect on the electronic spectrum of charge carrier and optical properties of materials [20,21]. Morphology also modifies the strength of the electron-hole Coulomb coupling due to the small dielectric constant of the surrounding media increasing the exciton binding energy in layered materials [22]. In addition, layered materials significantly increase the specific surface area providing abundant reaction sites. In this regards, the delamination of layered CNs into ultrathin nanosheets has proved to an effective method to enhance photocatalytic efficiency both via the exposure of reaction active sites and optimizing of light harvesting, charge separation and percolation. According to a predominance of intra-planar transport together with possible inter-planar transitions [23,24], a possible electron transport model is also depicted in Fig. 1. The singlet Frenkel excitons or polaronic charge carriers in conjugated polymers are most probable mobile species for electron transport in polymeric carbon nitride and their electronic transport is predominantly perpendicular to the layer. Consequently, single or a few layered two-dimension CNs is favorable for photocatalysis.

* Corresponding author.

E-mail address: hqfan@nwpu.edu.cn (H. Fan).

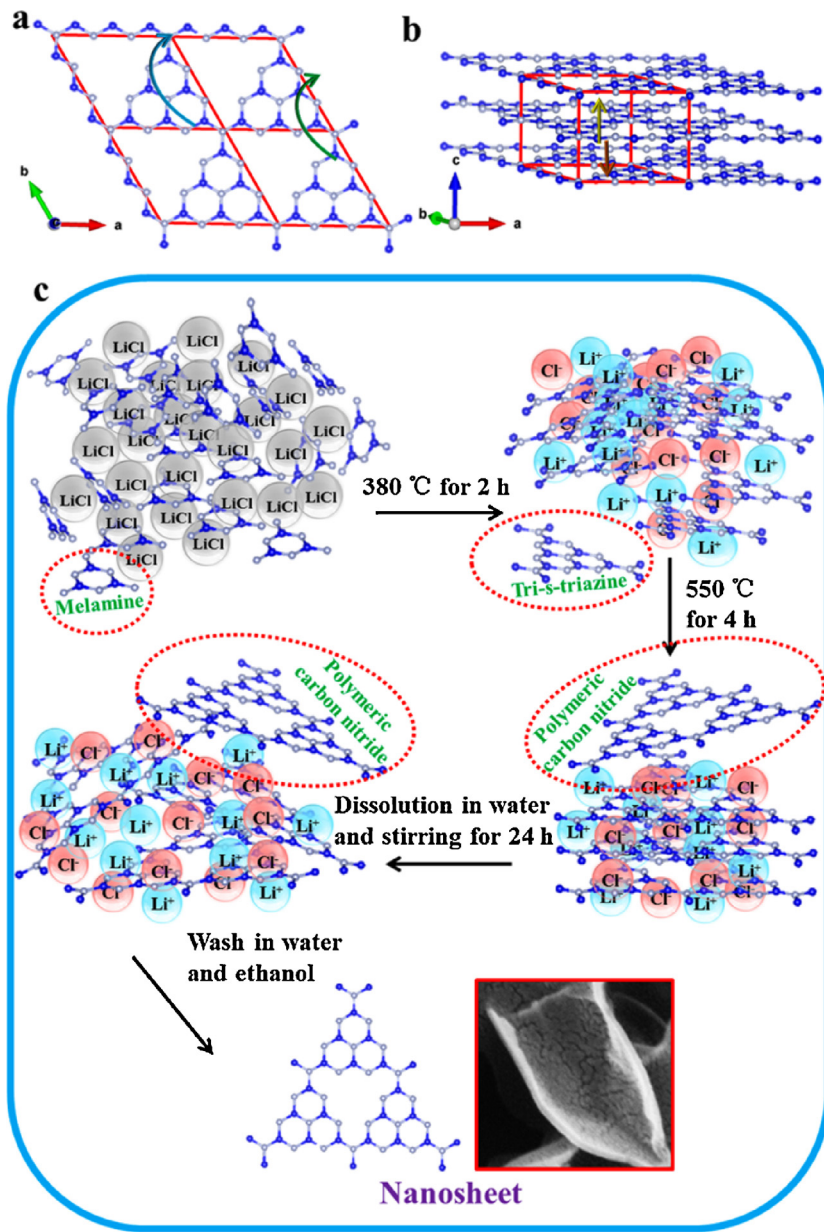


Fig. 1. Idealized CN structure viewed along (a) the c-axis and (b) the slightly tilted b-axis. Probable hopping transport scenarios are depicted: intra-planar (blue and green line), or inter-planar (yellow line) (c) Schematic illustration of the formation of bulk-CN/Li⁺ Cl⁻ and exfoliation process. The carbon atoms are blue and the nitrogen atoms are gray in atomic model. The units in synthesis process are depicted in red dotted circle. (For interpretation of the references to colour in this figure legend, the reader is referred to the web version of this article.)

Immense efforts have been made to achieve 2D layered graphitic polymeric carbon nitrides ($\text{g-C}_3\text{N}_4$, remarked as CN) previously. For example, Yang et al. exfoliate bulk $\text{g-C}_3\text{N}_4$ using continuous sonication-assisted liquid method [25]. Niu et al. synthesize $\text{g-C}_3\text{N}_4$ nanosheet utilizing thermal oxidation [26]. Li et al. prepare porous $\text{g-C}_3\text{N}_4$ by chemical oxidation [27]. However, those methods require complex procedure, long-time ultrasonic synthesis (10–16 h), high-temperature oxidation or strong oxidants.

Herein, we reported a two-step method to obtain porous carbon nitride nanosheets. It indicates the synthesis of porous carbon nitride nanosheets from bulk carbon nitrides by “green” liquid exfoliation in water without additives, toxic solvents or pre-intercalation steps in second step. Remarkably, the nanosheets with 2–3 nm in thickness and high density in-plane pores with 2–3 nm diameter exhibit superior photocatalytic efficiency for visible-light-driven hydrogen production from water splitting in comparison with bulk CNs.

2. Results and discussions

2.1. Material characterization

As depicted in Fig. 1c, the basis of this method is that the layered structure motifs (tris-s-triazine) forms via melamine rearrangements at round 380 °C for 2 h [28]. Lithium chloride loses crystal water at 380 °C and lithium chloride ions situate in channels running along the stacking direction. When the temperature increases to 550 °C, polymeric graphitic carbon nitride containing lithium chloride ions in inter-planar channels obtain and is marked as bulk-CN/Li⁺ Cl⁻. The efficiency of exfoliation will be highest, when the surface energy of solvent matches well with that of CNs [29]. According to zhang et al. calculation, the surface energies of CNs and water are 115 mJ/m² and ~102 mJ/m² respectively [30]. Therefore, water is a great candidate for exfoliation of bulk carbon nitrides. The bulk-CN/Li⁺ Cl⁻ is suspended in water (1 mg/mL) under vigorously

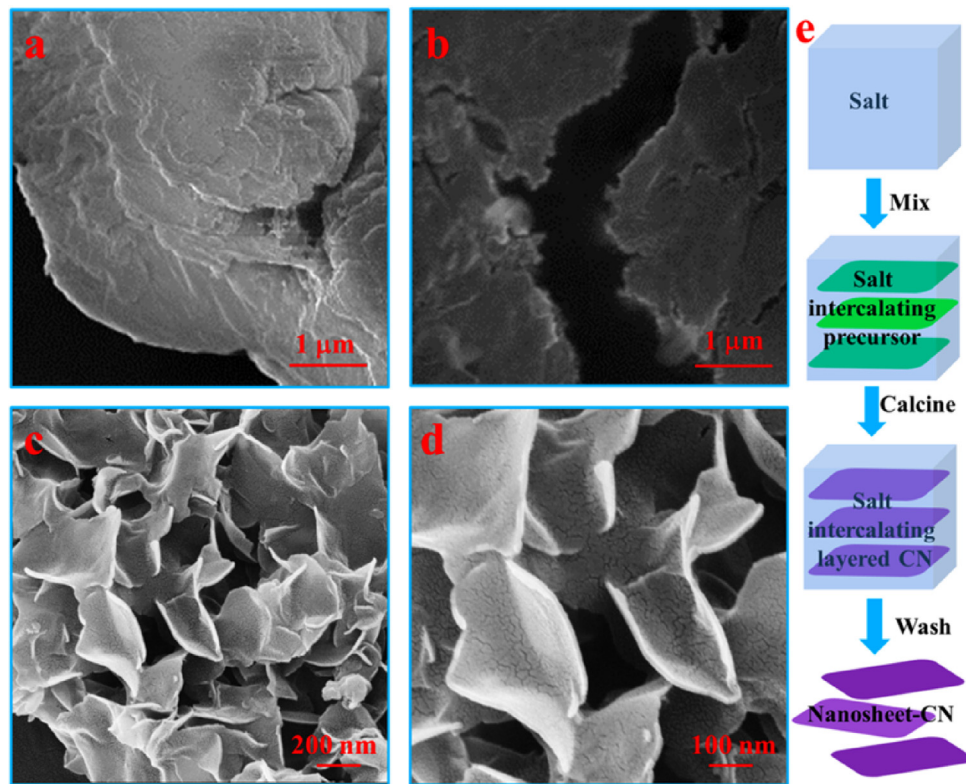


Fig. 2. SEM image of (a) bulk-CN, (b) bulk-CN/Li⁺ Cl⁻, (c) nanosheet-CN and (d) the nanosheets corresponding height image, (e) schematic of uniform CN nanosheets synthesis through water assisted exfoliation complex of 2D CNs and metal salt.

stirring for 24 h at room temperature. The aqueous suspensions are washed ten times with distilled water and ethanol respectively to remove lithium chloride ions. Finally, the nanosheets are precipitated by centrifugation at 8000 rpm.

Graphitic polymeric carbon nitride was synthesized by water assisted exfoliation of a complex through a single heating procedure using melamine and metal salt. In order to comparison, the bulk-CN is synthesized in the same condition except for no lithium chloride. The obtained graphitic polymeric carbon nitrides (denoted nanosheet-CN) are characterized by scanning electronic microscopy (SEM), transmission electronic microscopy (TEM) and atomic force microscopy (AFM). As shown in Fig. 2, bulk-CN is consisted of amounts of solid agglomerates with a size of several micrometers, while the bulk-CN/Li⁺ Cl⁻ is composed of fine aggregation and lithium chloride ions situate in channel of layered stack observed in the crack from Fig. 2b. The decrease of agglomerate size is assigned to the existence of lithium chloride. The melamine molecules are uniformly intercalated into intermediate layer of lithium chloride salts, which averts aggregating massive melamine to a particle. SEM image of layered products reveals nanosheets with lateral dimensions around a few hundred nanometers and thickness less than 5 nm. The nanosheets are very homogeneous on their surface and the shapes are quite regular without any patches (Fig. 2c and d). It indicates lithium chloride ions intercalate into inter-layers of CNs in the process of tri-s-triazine formation and polymerization. Moreover, the nanosheets can be easily collected by centrifugation. Furthermore, the EDS spectra and elemental mapping image were displayed in Fig.S1 and Fig.S2. The porous C₃N₄ nanosheets contained carbon, nitride and oxygen elements and the distribution of each element in edge of nanosheets was identical to that in plane. Comparing the bulk-CN and complex of CNs and metal salt, the probable mechanism of intercalation and exfoliation are depicted in Fig. 2e. In the first route, the melamine

was dispersed in the lithium chloride salt molecular. After calcination, then 2D CN nanosheets was formed on the intermediate layer of lithium chloride salt due to thermal polycondensation. In the second synthetic route, the nanosheets were separated by dissolving lithium chloride salt in deionized (DI) water owing to surface tension.

The TEM image (Fig. 3a and b) displays the very transparent features of layered CNs indicating the formation of 2D layered CN nanosheets. The nanosheet-CN is composed of a fewer atomic layer carbon nitride. From the TEM image of the edge of nanosheet, it can be seen amounts of 2–3 nm diameter regular in-plane pores through the whole nanosheet, which significantly increase the specific surface area. Fig. 3c displays the typical atomic force microscopic (AFM) image of layered carbon nitride nanosheets. The thickness analysis of the nanosheet-CN by AFM indicates an average thickness of around 2–3 nm. It clearly demonstrates that CN nanosheets have been successfully synthesized.

X-ray diffraction (XRD) patterns (Fig. 4a) confirm that the nanosheet shows reflection consistent with bulk-CN, which suggests that the addition of lithium chloride does not change the crystal structure. Two characteristic diffraction peaks of nanosheet-CN at 13.1° (100) and 27.9° (002) that are, respectively, assigned to the in-plane repeating unites of the continuous heptazine framework and the stacking of the conjugated aromatic structure with a spacing of ≈0.27 nm. The presence of (002) reflection shows right-shift from 27.4° to 27.9° indicating a 0.07 nm decreased stacking distance between the basic layered structure in the nanosheets [31,32]. In our case, the intercalation of lithium chloride ions leads to a denser packing, which thus shortens the gallery distance.

The identity of nanosheets can be further confirmed by using FT-IR spectroscope (Fig. 4b). The characteristic IR spectrum of the nanosheets is significantly consistent with that of bulk materials. The broad peaks between 3500 and 3000 cm⁻¹ can be attributed

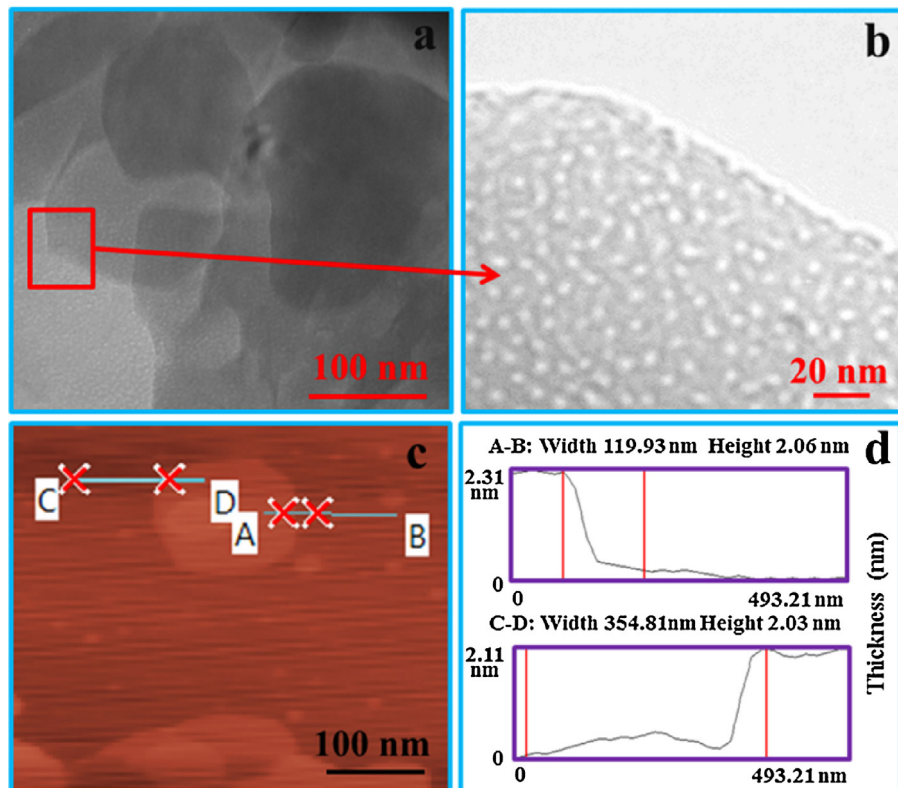


Fig. 3. TEM images of (a) nanosheet-CN and (b) the edge area of nanosheet. (c) AFM image of nanosheet-CN deposited on the mica wafer substrate, (d) the height curve determined along the line between A-B and C-D.

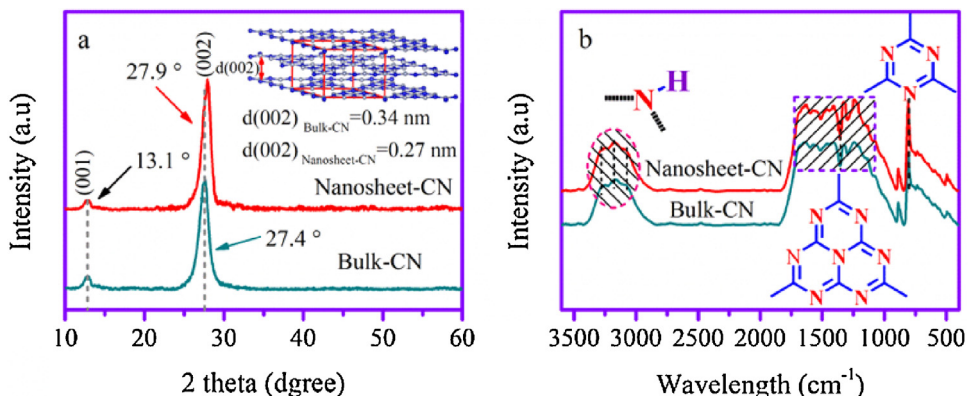


Fig. 4. (a) X-ray diffraction pattern and (b) FT-IR spectra of bulk-CN and nanosheet-CN.

to N–H stretches suggesting the partial hydro-generation of N atoms in the nanosheets. A band at 810 cm^{-1} stemming from triazine ring sextant out of plane bending and a Figureprint region at $1200\text{--}1620\text{ cm}^{-1}$ originating from tri-s-triazine are dominant by the same $\nu(\text{C}=\text{N}-\text{HC})$ and $\nu(\text{C}=\text{N})$ stretching vibrations [33]. Compared to bulk materials, these peaks become sharply, because the more ordered packing of hydrogen-bond cohered along strands of polymeric melon motifs forms during intercalation process [26]. It can increase electronic transport ability in intra-plane, consequently reducing recombination of charge carrier in electronic transmission process.

To further probe the chemical composition and chemical state of bulk-CN and nanosheet-CN, X-ray photoelectric spectroscopy was carried out. It could be seen both materials were examined for selected elements, namely, carbon, nitrogen and oxygen (Fig. 5a). The bulk-CN and porous nanosheet-CN were dispersed in water and the suspension of bulk-CN and porous nanosheet-CN were

both negatively charged, with a zeta potential of about 29.3 mV and 30.8 mV respectively indicating that both carried highly negative surface charge (Fig.S3). Hence, the Li^+ and Cl^- were completely eliminated after water exfoliation and lots of washing procedure. The high-resolution C 1s and N 1s spectra are developed into three peaks by Gaussian–Lorentzian fitting, respectively. As displayed in Fig. 5b and 5c, no evident binding energy shift of C 1s and N 1s core electrons implies that the chemical states of both carbon and nitrogen in the nanosheets are consistent with bulk materials. The peak centered at 288.16 eV make immense contribution to C1s spectra, which originated from sp^2C atoms bonded to N atoms inside the aromatic structure, while the peak at 286.02 eV is assigned to sp^2C atoms attached to the $-\text{NH}_2$ group in the aromatic ring [34]. The peak (284.6 eV) originating from graphitic $\text{sp}^2\text{C}=\text{C}$ gets strong suggesting more C atoms in nanosheets. For N 1s spectra, the peaks at binding energy of 398.60 and 400.66 eV are attributed into sp^2N atoms in triazine rings and bridging N atoms in tertiary nitro-

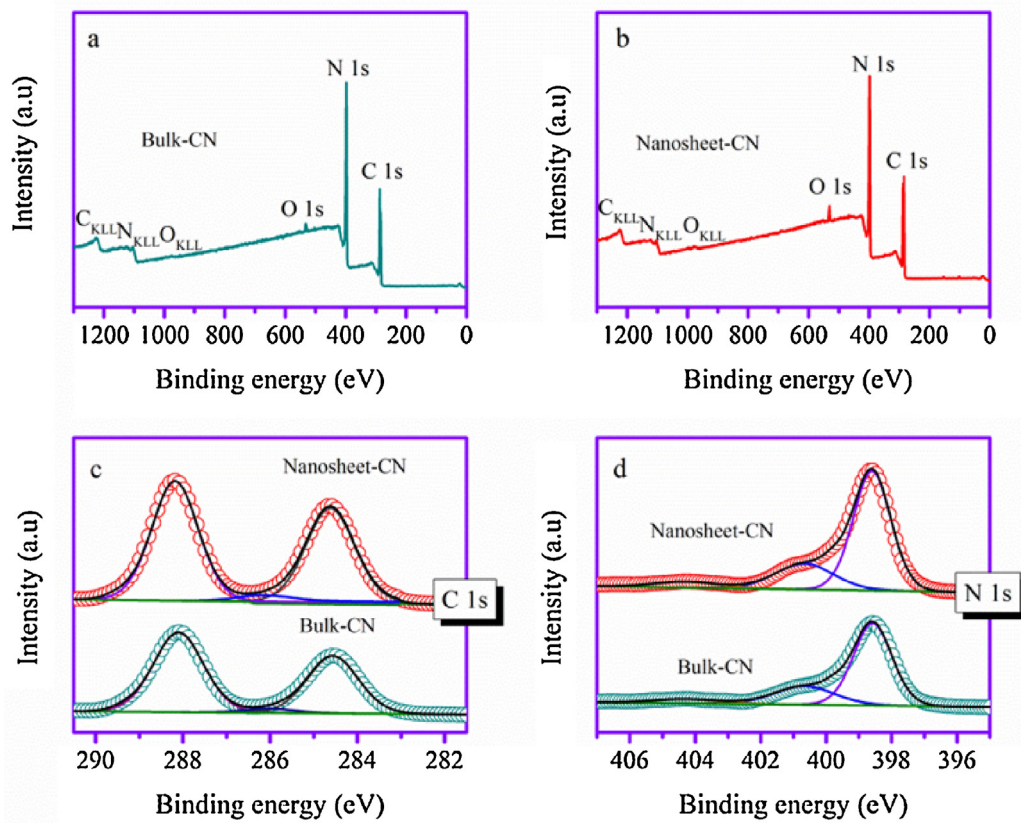


Fig. 5. XPS survey spectra for (a) bulk-CN and (b) nanosheet-CN. XPS spectra for (c) C 1s and (d) N 1s.

gen ($N-(C)_3$) or terminal amino functions (NH bonds)(NH bonds) respectively. The weak peak shows the charging effects or positive charge localization in heterocycles and the $-CN$ group [35]. According to the percentages of carbon and nitride determined by XPS analysis, the surface atomic ratio of C/N increases from pristine 0.73 (for the bulk-CN) to 0.78 (for the CN nanosheets), both of which are close to the ideal polymeric graphitic carbon nitride composition (0.75).

A larger surface area of photocatalyst is favorable for photocatalytic reaction, which can provide abundant reaction sites [36]. The possible contribution of increased surface from $9.8\text{ m}^2\text{ g}^{-1}$ for bulk-CN to $186.3\text{ m}^2\text{ g}^{-1}$ for nanosheet-CN is assessed by nitrogen adsorption-desorption isotherms. The shape of the isotherm for the nanosheets is remarkably different from that of bulk materials (Fig. 6). Compared to bulk-CN, a sharp rise in isotherm for nanosheets occurs at relative pressure higher 0.8 demonstrating the presence of abundant pores in the surface of products, which can offer a mass of reactivity sites. It makes obvious contribution to the enhancement of photocatalytic activity. The pore size distribution based on nonlocal density functional theory (NLDFT) method exhibits the existence of mesopores from 2 to 3 nm, which is in good agreement with TEM analysis. Indeed, the involvement of lithium chloride salt could strongly interact with dicyandiamide and in situ turn the polymerization way during the high temperature calcination process. The incorporation of Li and Cl atoms (larger than C and N atoms) as intercalating motifs could disturb the structure of carbon nitride, akin to the heteroatom-assisted “bottom-up” synthesis of CN nanosheets.

2.2. Electrochemical properties

To gain more insights into the electronic structure of nanosheets relative to bulk-CN, we perform UV-vis absorption spectra in

Fig. 7a. It indicates that the intrinsic absorption edge of CNs shows a blue-shift upon exfoliation into nanosheets. The almost exactly parallel characteristics of the absorption edge of resultant nanosheet-CN to that of bulk-CN strongly suggests the nature of band-to-band excitation in nanosheets. The bandgaps of bulk-CN and nanosheet-CN determined are 2.66 eV and 2.82 eV respectively. It is further confirmed that the intrinsic fluorescence emission peak shifts from 2.72 eV to 2.88 eV by lithium chloride exfoliation (Fig. 7b). Both declare the enlarged bandgap of CN nanosheets. The reason for this larger bandgap is assigned to the quantum confinement effect caused by shifting the conduction band and valence band edges along the opposite directions.

To confirm relative position of conduction band (CB) and valence band (VB), total densities state of VB and Motte-Schottky plots are carried out. From Fig. 7c, compared to bulk-CN, nanosheet-CN shows a VB maximum up-shift from 1.38 eV to 1.15 eV, as well as the VB being widened (0.16 eV). Interestingly, the VB up-shift 0.23 eV does not couple with the 0.23 eV increase of bandgap (0.16 eV increase), indicating the up-shift of CB. The Motte-Schottky plots further confirm that CB minimum simultaneously, emerges up-shift from 1.28 eV to 1.67 eV as observed in Fig. 7d. The increase of VB width narrows the distance of potential between carbon nitrides and water, enhancing the redox ability of charge carriers.

As shown in Fig. 7b, the PL emission peaks of CNs originating from radiative recombination of charge carriers become weak upon nanosheets indicating a suppressed recombination of photo-induced electron-hole pairs and more efficient electron transfer process in layered nanosheets. The Electronic conduction behavior is further investigated by typical I-V curves of bulk powder and nanosheet (Fig. 8a). There is no apparent current is detected under applied bias from -3 V to 3 V for bulk CNs suggesting the extremely poor ability of electronic transport. For nanosheet, a typical semiconducting I-V curve is achieved indicating a great

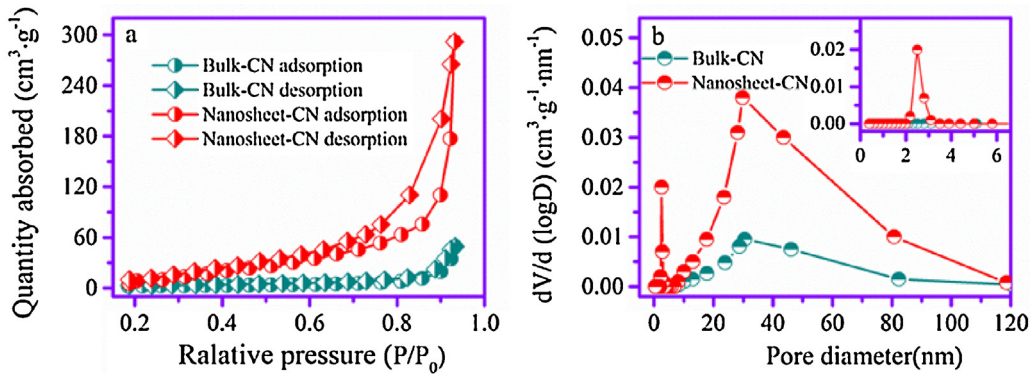


Fig. 6. (a) Nitrogen gas adsorption-desorption isotherm of bulk-CN and nanosheet-CN and (b) the corresponding pore size distribution curve.

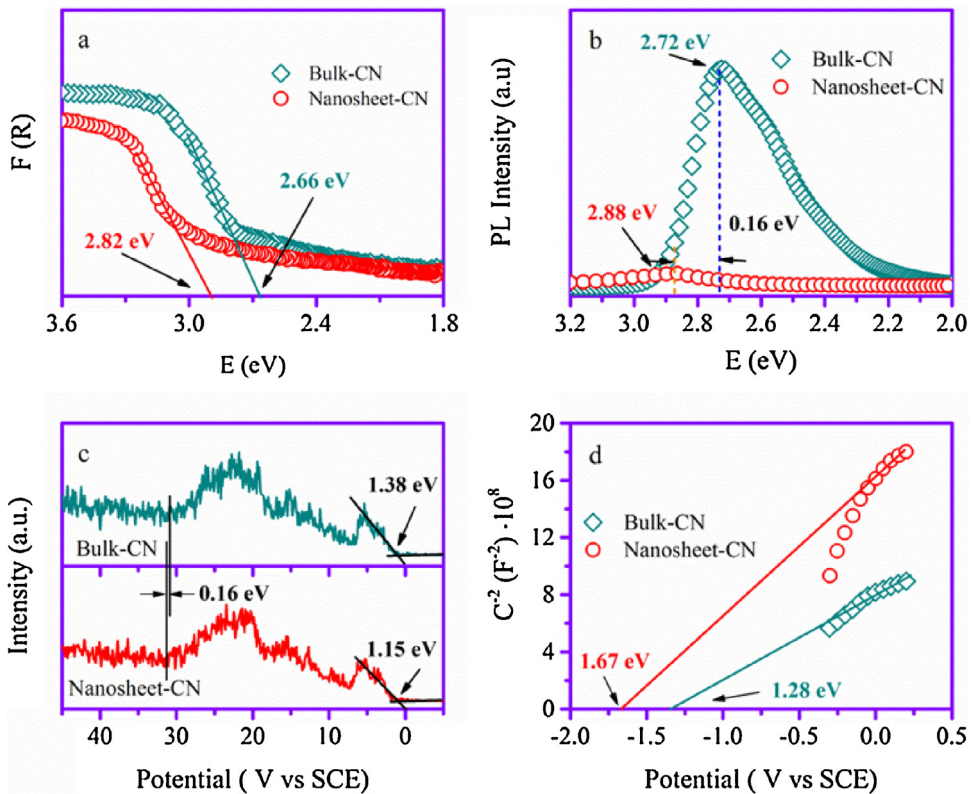


Fig. 7. (a) UV-vis absorption of bulk-CN and nanosheet-CN spectra, (b) fluorescence emission spectra of bulk-CN and nanosheet-CN recorded at 298 K, (c) total densities of states of XPS valence band spectra, (d) electrochemical Motte-Schottky plots at frequency of 1k Hz.

electron transport along the in-plane direction in the nanosheet. The layer in nanosheet, dominantly composed of hydrogen-bond cohered strands of polymeric melon motifs plays an important role of electron transport channel, whereas the layer in bulk materials consisted of isolated small strands block electronic transport in I-V measurement process. With respect of bulk CNs, photo-induced charge carrier can reach the surface of photocatalyst along in-plane direction in nanosheets owing to superior ability of electronic transport, which reduces the recombination of electrons-holes. Hence, we envisage the nanosheets can exhibit superior photocatalytic activity.

To further probe the charge carrier density in CN nanosheets, Mott-Schottky plots based on capacitances originating from the electrochemical impedance measured at potential at 1 kHz frequency are performed [37] (Fig. 8b). The charge carrier density is calculated according the follow equation [38]:

$$N_D = 2/(e\epsilon\epsilon_0 m) \quad (1)$$

where N_D is the charge carrier density, e is the elementary electron charge, ϵ_0 is the permittivity in vacuum, ϵ is the dielectric constant, and m is the slope of the C^{-2} vs potential plot. The slopes of bulk CNs and nanosheet are 2.58×10^9 and 4.03×10^8 respectively. Therefore, the charge carrier density of nanosheet is upgraded to five times than that of bulk materials. This high charge carrier density in CNs nanosheets can facilitate charge carriers transfer, which is favorable for the contact between photo-induced charge and water molecular and subsequently enhances the photocatalytic performance.

To identify the effects of exfoliation on the electrochemical performance, the electronic transport kinetics are evaluated by using the electrochemical impedance spectra (EIS). There is a well-fitting semicircle in high frequency region and middle-frequency region, and the diameter of the semicircle is approximately assigned to the charge-transfer resistance. Remarkably, the nanosheet electrode exhibits much smaller resistance than bulk CNs, implying a

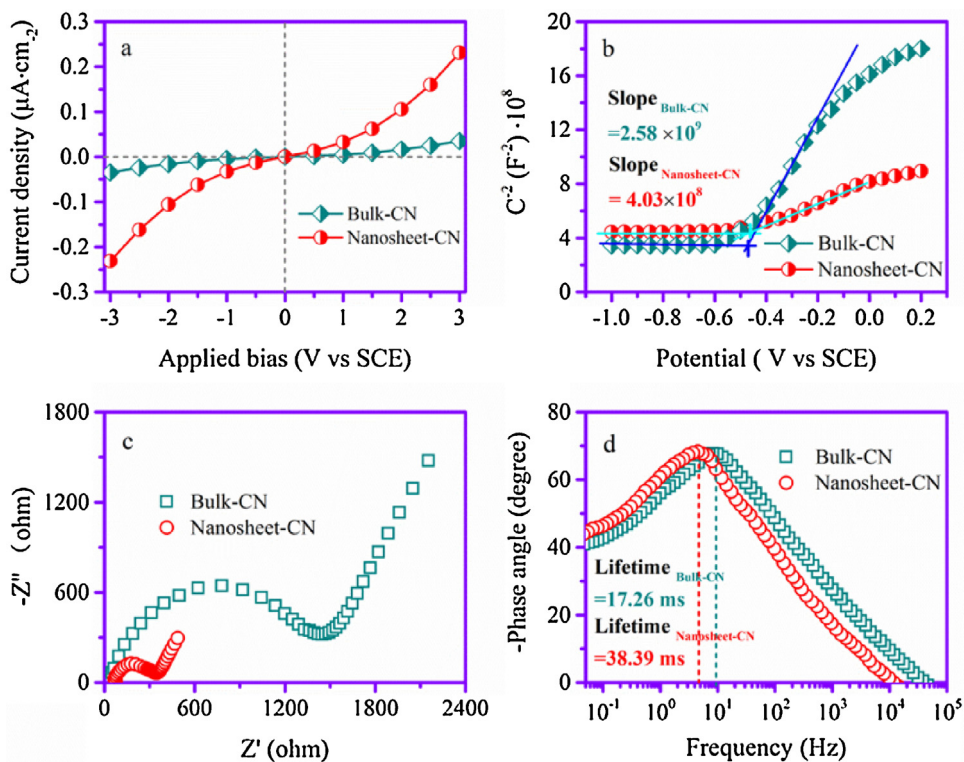


Fig. 8. (a) typical I–V curves of bulk-CN and nanosheet electrodes in 0.5 M Na_2SO_4 aqueous solution, (b) the electrochemical Motte–Schottky plots at frequency of 1 kHz in 0.5 M Na_2SO_4 aqueous solution, (c) EIS Nyquist plots and (d) Bode phase plots of bulk-CN and nanosheet-CN, investigated by applying a sine wave current at frequency from 1 MHz to 0.01 Hz in 0.5 M Na_2SO_4 aqueous solution.

better electrochemical activity for nanosheets [39] (Fig. 8c). The layered CN nanosheets significantly accelerate the electron transfer process, which in turn enhances the separation efficiency of photo-induced charge carriers. In order to investigate the effect of the CNs-electron lifetime on the impedance spectra, Blot plots of bulk-CN and nanosheet are built in Fig. 8d. Layered materials possessing superior electron mobility can suppress recombination process, thus increasing the electron lifetime in nanosheets [40]. Compared to bulk CNs electrode, the mid-frequency characteristic peak of nanosheet electrode shifts slightly to a lower frequency (from 8.31 Hz to 4.50 Hz). The shift of characteristic peak to lower frequency reveals a more rapid electron mobility process [41]. The lifetime of electrons τ_{eff} can be extracted by the following equation [42]:

$$\tau_{\text{eff}} \approx 1/\omega_{\text{min}} = 1/2\pi f_{\text{min}} \quad (2)$$

The electron lifetime is only determined by the minimum frequency (ω_{min}) of the mid-frequency. In actual calculation, we reverse the minimum frequency (f_{min}) of Blot plots peak as the function of electron lifetime. Specifically, the electron lifetime for nanosheet (38.39 ms) is around two times higher than that of bulk materials (17.26 ms). Thus, the exfoliation from bulk CNs to layered structure, facilitate the electron transport. The improvement electron transfer accelerates photocatalytic reaction.

The time-resolved fluorescence decay spectra (Fig. 9) of bulk-CN and nanosheet-CN, is recorded to investigate the photo-physical behavior of photo-induced charge carrier. The fluorescent intensities of both materials decay exponentially and can be depicted according following equations [43,44]:

$$n(t) = K_1 \exp(-t/\tau_1) + K_2 \exp(-t/\tau_2) + K_3 \exp(-t/\tau_3) \quad (3)$$

where, $n(t)$ is the concentration of charge carrier, τ_1, τ_2, τ_3 were the lifetime of charge carrier, K_1, K_2, K_3 were constant. The nanosheet-

Table 1

The radiative fluorescence lifetimes and their relative percentages of photoexcited charge carriers in the bulk –CN and nanosheet-CN.

Samples	Component	Lifetime (ns)	Intensity (%)
Bulk-CN	τ_1	0.09	12.94
	τ_2	3.06	51.01
	τ_3	11.20	36.05
Nanosheet-CN	τ_1	1.02	21.69
	τ_2	5.16	47.63
	τ_3	31.76	30.68

CN displays slow decay kinetics. Fitting the decay spectrum shows three radiative lifetimes with different percentages as given in Table 1. In detail, the shortest lifetime of 0.09 ns in the bulk-CN increases to 1.02 ns in the nanosheet-CN and its percentage increases from 12.94% to 21.69%. The medium lifetime and percentage of charge carrier increase from 3.06 ns for 51.01% in bulk-CN to 5.16 ns for 47.63% in nanosheet-CN. The longest lifetime of nanosheet-CN is up to 31.76 ns, about 20.56 ns longer than bulk-CN (11.20 ns) through its percentage decreases from 36.05% to 30.68%. Furthermore, compared to bulk-CN, the average electron lifetime of nanosheet-CN is significantly prolonged (6.8 ns) (Fig. 9b). The prolonged lifetime is related to the enhanced electron transport and/or electronic band structure changes induced by quantum confinement effect. Moreover, the prolonged lifetime increases the probability of photo-induced electrons and holes that are captured by reactive materials and able to run photo-redox functions. The results are consistent with electrochemical impedance spectra.

2.3. Hydrogen evolution performance

The photocatalytic activity is dominantly determined by the generation of photo-induced electrons–holes pairs. As shown in Fig. 10, under the visible light irradiation, the electrons of CNs jump

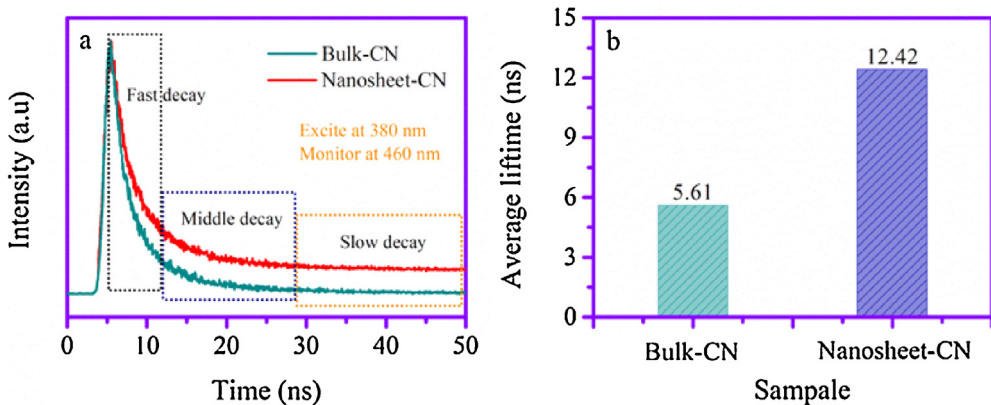


Fig. 9. (a) Time-resolved fluorescence decay spectra and (b) average electron lifetime of bulk-CN and nanosheet-CN monitored at 460 nm by time-correlated single-photon counting. The products are excited by the incident light of 380 nm from a picosecond pulsed light-emitting diode at room-temperature. The insert is the radiative fluorescence lifetimes and their relative percentages of photo-induced charge carriers in the bulk-CN and nanosheet-CN.

from VB to CB. Then, the photo-generated electrons transfer to the surface of photocatalyst, and couple with Pt particles. The hydrogen ions accept electrons to product hydrogen, while holes react with sacrificial agent through oxidation. Obviously, the quantity and mobility of photo-generated charge carriers dominate the photocatalytic activity. Compared bulk CNs, nanosheets possess enlarged bandgap originating from VB and CB shifting along opposite direction, which leads to width VB and higher CB minimum resulting in strong redox ability. **Fig. 10a** displays the transient photocurrent response of as-synthesized product layers printed on indium tin oxide (FTO) glass plates in a 0.5 M Na_2SO_4 aqueous solution under 150 W Xe lump light irradiation ($\lambda > 400$ nm). The photocurrent generated from nanosheet electrode is much higher than that from bulk material electrode. Hence, the nanosheets modified electrodes had steady photoelectrochemical performance under visible light irradiation. In addition, the transient photocurrent is widely regarded as the most efficient evidence to characterize charge separation. The higher generation of photocurrent on nanosheet electrode owing to a better electron transfer rate indicates that CN nanosheets have an advantage for a superior photocatalytic performance.

The different sacrificial agents and different deposited-Pt content make different contributes to photocatalytic performance. From **Fig. 10b** and c, the photocatalytic performance of CN nanosheets is up to maximum, when it is carried out in aqueous solution containing 10 vol% triethanolamine (TEOA) as sacrificial agent and 0.6% deposited-Pt as co-catalyst. Therefore, the follow photocatalytic reactions are operated in this condition.

Owing to smaller material size, thus, higher exposed surface area and possibly more abundant photoactive sites, the CN nanosheets are tested for photocatalytic hydrogen evolution and compared to the water reduction activity of the bulk material. The photocatalytic activity of the CN nanosheet suspension and the bulk material is measured in aqueous solution containing 10 vol% triethanolamine (TEOA) solution under visible light irradiation. Under $\lambda > 400$ nm, the stable hydrogen evolution for nanosheet ($107.84 \mu\text{mol h}^{-1}$) is observed from photo-reductive water splitting at a rate more six times higher than that observed from bulk CNs ($16.31 \mu\text{mol h}^{-1}$) (**Fig. 10d**). The durability of CN nanosheets acting as photocatalysts for hydrogen production is evaluated by four consecutive operations. As depicted in **Fig. 10e**, the hydrogen produced increases steadily with irradiation time, without evident deactivation after the fourth cycle experiments. Meanwhile, the wavelength dependent hydrogen production is performed on layered CN nanosheets (**Fig. 10f**). The trend of hydrogen production is exactly matched with optical absorption of the nanosheet photo-

catalyst implying that the hydrogen production reaction is indeed induced by the excitation of the nanosheets [9]. The comparison with other reported carbon nitrides for hydrogen production is shown in Table S1. Photocatalytic activity of as-synthesized carbon nitride nanosheets is significantly superior to those previously reported. In fact, the water-assisted ion-intercalated exfoliation can drastically improve photocatalytic performance. Importantly, this method is simple, environmental friendly and cost-efficient.

As shown in **Fig. 11 a**, the CN nanosheet photocatalyst collected after photocatalytic hydrogen evolution reaction for 24 h shows an unchanged crystal structure, indicating the porous CN nanosheets from in situ lithium chloride ions intercalating bulk CN as photocatalyst being stable. In addition, the PL spectra of catalyst after photocatalytic reaction are determined in **Fig. 11b**. The quenching of the photoluminescence behavior showed suppressed recombination of photo-induced carriers and more efficient electron transfer process, indicating the Pt nanoparticles are successfully deposited on the surface of CN nanosheets. It displays the potential application of these nanosheets as a substrate for loading other catalysts. **Fig. 11c** and d depict the photocatalytic mechanism and electron transfer path of Pt modified-CN nanosheets. The Pt nanoparticles make great contributes to separation of electrons and holes and remarkably enhance the visible light photocatalysis for water splitting to product hydrogen.

2.4. Mechanism and discussion

The probable photocatalytic mechanism of CNs for hydrogen evolution from water splitting with triethanolamine (TEOA) as electron donor and deposited-Pt as co-photocatalyst under visible-light and the schematic electronic structure for remarkably improving photocatalytic activities are illustrated in **Fig. 12** and the comparison of bulk-CN and nanosheet-CN is displayed in **Table 2**. Under the excitation of visible light, the electrons originating from CNs jump from VB to CB. The photo-generated electrons transfer to the surface of CNs, and couple with Pt particles. The hydrogen ions accept coupled-Pt electron to product hydrogen, while the holes react with TEOA through oxidation. The synergistic effects of larger surface area, enhanced electronic transport, enlarged absorption bandgap, prolonged electron lifetime, lowered recombination of photo-excited charge carrier and increase charge carrier density, is beneficial for the remarkable hydrogen production. Compared to bulk-CN, the nanosheet-CN composed of thickness nanosheets possesses larger surface area providing abundant photoactivity site for reactant molecular and enhances electronic transport resulting in substantially low bulk recombination of charge carrier. Impor-

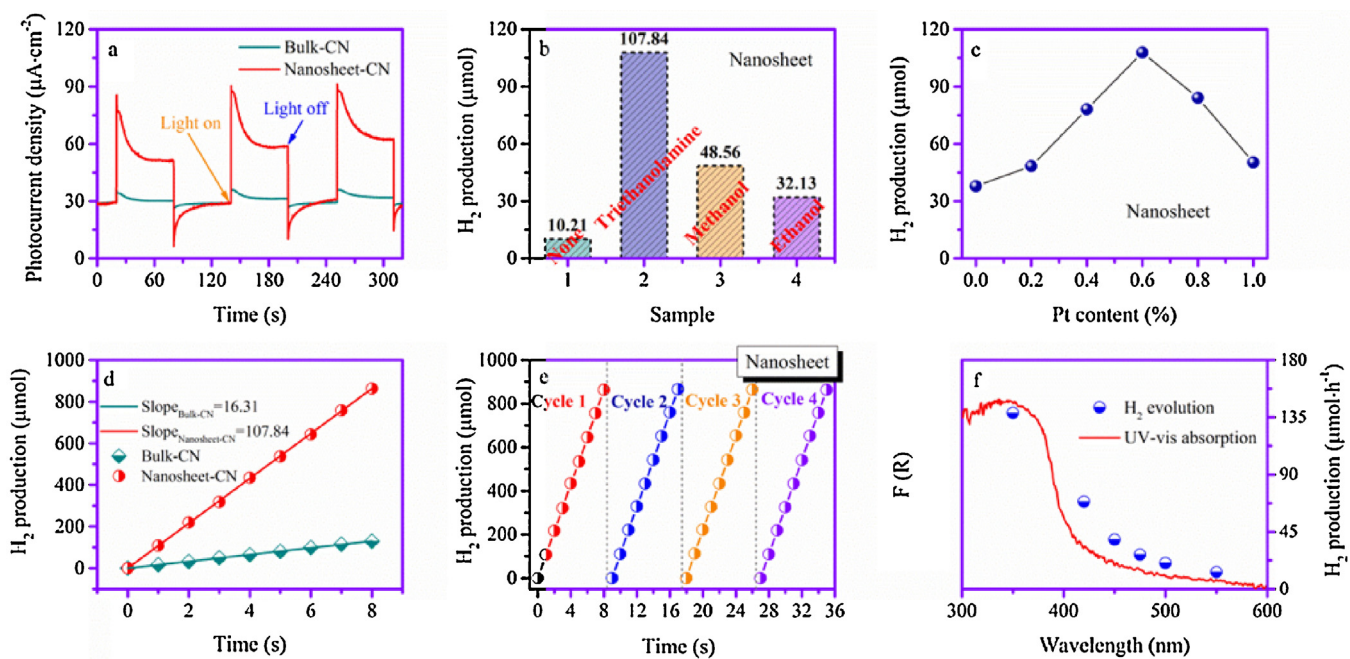


Fig. 10. (a) Periodic on/off photocurrent responses under 150 W Xe lump light irradiation at bulk-CN and nanosheet-CN electrodes in 0.5 M Na_2SO_4 solution without any bias potential. The photocatalytic activity of porous nanosheet-CN (b) the H_2 production from aqueous solution containing 10 vol% different scavengers, (c) different contents of deposited-Pt as co-catalyst. (d) The H_2 production from aqueous solution containing 10 vol% triethanolamine scavenger as electron donor and 0.6% deposited-Pt as co-catalyst, the fitting linear is used to express the average H_2 evolution per hour. (e) The durability test of nanosheet photocatalyst, (f) the wavelength dependence of H_2 production by CN nanosheets. For comparison, UV-vis absorption spectrum of nanosheet-CN is also given.

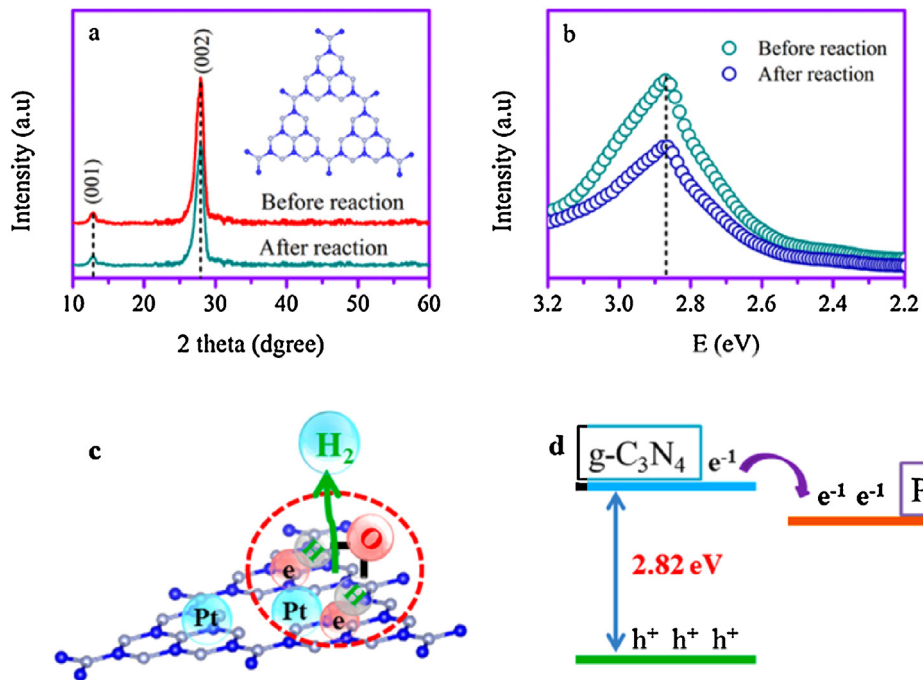


Fig. 11. (a) The XRD pattern and (b) PL spectra of porous nanosheets-CN before and after reaction. (c) The mechanism of photocatalytic reaction of deposition Pt on the surface of nanosheet-CN, (d) the electron transfer in the process of photocatalytic reaction.

Table 2

Comparison of bulk-CN and nanosheet-CN.

	Stacking distance	Specific surface area	Bandgap	Valence/conduction bandgap	Average electron lifetime	Photocatalytic performance
Bulk-CN	0.34 nm	$9.8\text{m}^2\text{g}^{-1}$	2.66 eV	1.38/1.28 eV	5.61 ns	$16.31\text{\mu mol h}^{-1}$
Nanosheet-CN	0.27 nm	$186.3\text{m}^2\text{g}^{-1}$	2.82 eV	1.15/1.67 eV	12.42 ns	$107.84\text{\mu mol h}^{-1}$

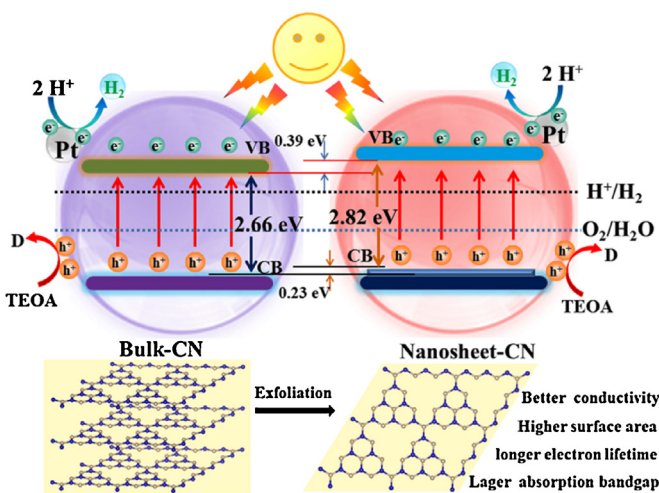


Fig. 12. Schematic illustration of visible-light photocatalytic performance of Pt-deposited bulk-CN and nanosheet-CN, TEOA is triethanolamine and D is oxidation products.

tantly, as quantum confinement effects, the increasing intrinsic bandgap and width of valence improve the redox ability of charge carrier. The prolonged lifetime has a significant contribution to promoting photoactivity under visible-light or UV-vis light. In fact, the water-assisted ion-intercalated exfoliation CNs can drastically improve photocatalytic performance. Importantly, this method is simple, environmental friendly and cost-efficient.

3. Conclusions

In conclusion, polymeric carbon nitride nanosheets are successfully synthesized by a simple, environmental friendly and cost-efficient aqueous exfoliation procedure starting with bulk CN/Li⁺ Cl⁻ fabricated by lithium chloride ions intercalation in dicyandiamide polycondensation process. The thickness of the nanosheets is 2–3 nm and the mesopores with 2–3 nm diameters on their surface of the nanosheets are very homogeneous. The photocatalytic activity of the exfoliated products is superior by a factor of more six to bulk CN materials. The remarkable photocatalytic performance of the layered carbon nitride nanosheets is considered to be a synergistic consequence of higher surface area providing abundant active sites, superior electron mobility accelerating electron transport and reducing recombination of photo-induced charge carriers, enlarged bandgap enhancing redox ability and prolonged electron lifetime offering more opportunities to photocatalytic reaction. These characteristics are highly efficient in promoting visible light responsive photo-oxidation and photo-reduction processes. This materials in envisaged to photocatalysis and photovolta to solve global crisis of environmental issue and energy shortage.

Acknowledgements

This work was supported by the Natural Science Foundation (51172187), the SPDRF (20116102130002) and 111 Program (B08040) of MOE, the Xi'an Science and Technology Foundation (CXY1510-2), the NPU Graduate Seeding Foundation and SKLP Foundation (KP201421), and the Fundamental Research Funds for the Central Universities (3102014JGY01004) of China.

Appendix A. Supplementary data

Supplementary data associated with this article can be found, in the online version, at <http://dx.doi.org/10.1016/j.apcatb.2016.03.002>.

References

- [1] M.G. Walter, E.L. Warren, J.R. McKone, S.W. Boettcher, Q. Mi, E.A. Santori, N.S. Lewis, *Chem. Rev.* 110 (2010) 6446–6473.
- [2] A.A. Bakulin, A. Rao, V.G. Pavelyev, P.H.M. van Loosdrecht, M.S. Pshenichnikov, D. Niedzialek, J. Cornil, D. Beljonne, R.H. Friend, *Science* 335 (2012) 1340–1344.
- [3] Y. Wang, X. Wang, M. Antonietti, *Angew. Chem. Int. Ed.* 51 (2012) 68–89.
- [4] Y. Zheng, J. Liu, J. Liang, M. Jaroniec, S.Z. Qiao, *Energy. Environ. Sci.* 5 (2012) 6717–6731.
- [5] X. Bai, L. Wang, R. Zong, Y. Zhu, *J. Phys. Chem. C* 117 (2013) 9952–9961.
- [6] Y. Zheng, L. Lin, B. Wang, X. Wang, *Angew. Chem. Int. Ed.* 127 (2015) 13060–13077.
- [7] G. Aligara-Siller, N. Severin, S.Y. Chong, T. Björkman, R.G. Palgrave, A. Laybourn, M. Antonietti, Y.Z. Khimyak, A.V. Krasheninnikov, J.P. Rabe, U. Kaiser, A.I. Cooper, A. Thomas, M.J. Bojdys, *Angew. Chem. Int. Ed.* 53 (2014) 7450–7455.
- [8] J. Fang, H. Fan, M. Li, C. Long, *J. Mater. Chem. A* 3 (2015) 13819–13826.
- [9] H.B. Tao, H.B. Yang, J. Chen, J. Miao, B. Liu, J. Beilstein, *Nanotechnology* 5 (2014) 770–777.
- [10] X. Yang, H. Tang, J. Xu, M. Antonietti, M. Shalom, *Chem. Sus. Chem.* 8 (2015) 1350–1358.
- [11] X. Yang, Z. Chen, J. Xu, H. Tang, K. Chen, Y. Jiang, (2015) 15285–15293.
- [12] J. Zhang, M. Zhang, R. Sun, X. Wang, *Angew. Chem. Int. Ed.* 51 (2012) 10145–10149.
- [13] Y. Lu, D. Chu, M. Zhu, Y. Du, P. Yang, *Phys. Chem. Chem. Phys.* 17 (2015) 17355–17361.
- [14] X. Zhang, T. Peng, L. Yu, R. Li, Q. Li, Z. Li, *ACS. Catal.* 5 (2015) 504–510.
- [15] H. Xu, J. Yan, X. She, L. Xu, J. Xia, Y. Xu, Y. Song, L. Huang, H. Li, *Nanoscale* 6 (2014) 1406–1415.
- [16] K. Schwinghammer, M.B. Mesch, V. Duppel, C. Ziegler, J. Senker, B.V. Lotsch, *J. Am. Chem. Soc.* 136 (2014) 1730–1733.
- [17] S. Yang, X. Feng, X. Wang, K. Müllen, *Angew. Chem. Int. Ed.* 50 (2011) 5339–5343.
- [18] X. Zhuang, Y. Mai, D. Wu, F. Zhang, X. Feng, *Adv. Mater.* 27 (2015) 403–427.
- [19] X. Bai, L. Wang, R. Zong, Y. Zhu, *J. Phys. Chem. C* 117 (2013) 9952–9961.
- [20] N.A. Gippius, A.L. Yablonskii, A.B. Dzyubenko, S.G. Tikhodeev, L.V. Kulik, V.D. Kulakovskii, A. Forchel, *J. Appl. Phys.* 83 (1998) 5410–5415.
- [21] K. Akatsuka, G. Takanashi, Y. Ebina, M. Haga, T. Sasaki, *J. Phys. Chem. C* 116 (2012) 12426–12433.
- [22] L.V. Kulik, V.D. Kulakovskii, M. Bayer, A. Forchel, N.A. Gippius, S.G. Tikhodeev, *Phys. Rev. B* 54 (1996) 2335–2338.
- [23] C. Merschjann, T. Tyborski, S. Orthmann, F. Yang, K. Schwarzburg, M. Lublows, M.C. Lux-Steiner, T. Schedel-Niedrig, *Phys. Rev. B* 87 (2013) 205204–205306.
- [24] T. Tyborski, C. Merschjann, S. Orthmann, F. Yang, M. Lux-Steiner, T. Schedel-Niedrig, *J. Phys. Condens. Mat.* 25 (2013) 1–7.
- [25] J. Xu, L. Zhang, R. Shi, Y. Zhu, *J. Mater. Chem. A* 1 (2013) 14766–14770.
- [26] P. Niu, L. Zhang, G. Liu, H. Cheng, *Adv. Funct. Mater.* 22 (2012) 4763–4770.
- [27] H.J. Li, B.W. Sun, L. Sui, D.J. Qian, M. Chen, *Phys. Chem. Chem. Phys.* 17 (2015) 3309–3315.
- [28] A. Thomas, A. Fischer, F. Goettmann, M. Antonietti, J. Müller, R. Schlögl, J.M. Carlsson, *J. Mater. Chem.* 18 (2008) 4893–4897.
- [29] Y. Hernandez, V. Nicolosi, M. Lotya, F.M. Blighe, Z. Sun, S. De, I.T. McGovern, B. Holland, M. Byrne, Y.K. Gun'ko, J.J. Boland, P. Niraj, G. Duesberg, S. Krishnamurthy, R. Goodhue, J. Hutchison, V. Scardaci, A.C. Ferrari, J.N. Coleman, *Nan. Nanotechnol.* 3 (2008) 563–568.
- [30] X. Zhang, X. Xie, H. Wang, J. Zhang, B. Pan, Y. Xie, *J. Am. Chem. Soc.* 135 (2013) 18–21.
- [31] Y. Wang, X. Wang, M. Antonietti, *Angew. Chem. Int. Ed.* 51 (2012) 68–89.
- [32] K. Schwinghammer, M.B. Mesch, V. Duppel, C. Ziegler, J. Senker, B.V. Lotsch, *J. Am. Chem. Soc.* 136 (2014) 1730–1733.
- [33] S. Yang, Y. Gong, J. Zhang, L. Zhan, L. Ma, Z. Fang, R. Vajtai, X. Wang, P.M. Ajayan, *Adv. Mater.* 25 (2013) 2452–2456.
- [34] A. Vinu, *Adv. Funct. Mater.* 18 (2008) 816–827.
- [35] Y. Cui, J. Zhang, G. Zhang, J. Huang, P. Liu, M. Antonietti, X. Wang, *J. Mater. Chem.* 21 (2011) 13032–13038.
- [36] G. Liu, C. Sun, H.G. Yang, S.C. Smith, L. Wang, G.Q.M. Lu, H. Cheng, *Chem. Commun.* 46 (2010) 755–757.
- [37] X. Lu, G. Wang, S. Xie, J. Shi, W. Li, Y. Tong, Y. Li, *Chem. Commun.* 48 (2012) 7717–7721.
- [38] H. Zhao, H. Yu, X. Quan, S. Chen, H. Zhao, H. Wang, *RSC. Adv.* 4 (2014) 624–628.
- [39] S. Wi, H. Woo, S. Lee, J. Kang, J. Kim, S. An, C. Kim, S. Nam, C. Kim, B. Park, *Nanoscale. Res. Lett.* 10 (2015) 6–8.
- [40] C. Cho, J.H. Moon, *Adv. Mater.* 23 (2011) 2971–2975.
- [41] S. Sun, L. Gao, Y. Liu, *Appl. Phys. Lett.* 96 (2010) 83113.
- [42] R. Kern, R. Sastrawan, J. Ferber, R. Stangl, J. Luther, *Electrochim. Acta* 47 (2002) 4213–4225.
- [43] Z. Ovadyahu, *Phys. Rev. B* 91 (2015) 094204–094208.
- [44] A. Winnerl, R.N. Pereira, M. Stutzmann, *Phys. Rev. B* 91 (2015) 075316–075329.